

Numerical Simulation of 2D and 3D Sloshing Waves in a Regularly and Randomly Excited Container

Eswaran M¹, Akashdeep S. Virk² and Ujjwal K. Saha^{3*}

1. Structural and Seismic Engineering Section, Reactor Safety Division, Bhaba Atomic Research Centre, Trombay, Mumbai 400085, India

2. Department of Mechanical Engineering, National University of Singapore, Singapore 119077, Singapore

3. Department of Mechanical Engineering, Indian Institute of Technology Guwahati, Guwahati 781039, India

Abstract: In this paper, various aspects of the 2D and 3D nonlinear liquid sloshing problems in vertically excited containers have been studied numerically along with the help of a modified σ -transformation. Based on this new numerical algorithm, a numerical study on a regularly and randomly excited container in vertical direction was conducted utilizing four different cases: The first case was performed utilizing a 2D container with regular excitations. The next case examined a regularly excited 3D container with two different initial conditions for the liquid free surface, and finally, 3D container with random excitation in the vertical direction. A grid independence study was performed along with a series of validation tests. An iteration error estimation method was used to stop the iterative solver (used for solving the discretized governing equations in the computational domain) upon reaching steady state of results at each time step. In the present case, this method was found to produce quite accurate results and to be more time efficient as compared to other conventional stopping procedures for iterative solvers. The results were validated with benchmark results. The wave elevation time history, phase plane diagram and surface plots represent the wave nonlinearity during its motion.

Keywords: 3D container; free surface; σ -transformation; sloshing wave; finite difference method; Numerical Simulation

Article ID: 1671-9433(2013)03-0298-17

1 Introduction

Liquid sloshing is one of the most severe problems in transportation. Sloshing has been defined as the free surface oscillations of liquid in a partially filled container. When a partially filled liquid container gets accelerated in one or more directions due to external forces, waves will occur on the liquid free surface. This type of sloshing is called externally induced sloshing. Sometimes, self induced sloshing also arises while transferring the liquid from one container to another. Most of the researchers have concentrated their efforts on externally induced sloshing because of its practical significance. The knowledge of liquid free surface natural frequencies is important in the design of liquid containers subjected to different types of

excitation (Maleki and Ziyaeifar, 2008; Ibrahim, 2005). The dynamic behavior of a free liquid surface or the severity of the sloshing depends on the type of excitation and the frequency content, type of fluid, container shape, liquid fill level, excitation amplitude, and direction of the container motion. Civil engineers and seismologists have been studying liquid sloshing effects on large dams, oil containers and elevated water towers under ground motion for years.

Sloshing can be broadly classified into two types; namely self-induced sloshing and externally induced sloshing, based on how sloshing is generated inside its container. The main difference is that, in self-induced sloshing, the container is motionless whereas, in externally induced sloshing, the container will move owing to external disturbances. In the case of externally induced sloshing, external force such as an earthquake or a sudden brake on a moving container vehicle acts as the excitation source for sloshing (Eswaran *et al.*, 2011). Many theoretical and experimental research studies have been carried out in the area of liquid sloshing in fixed and moving containers. In the past, Jacobson and Ayre (1951), and Graham and Rodriguez (1952) performed some basic studies relevant to this topic. Housner (1957, 1963) developed an analytical method for the determination of hydrodynamic wall pressures under the assumption that the container is a rigid structure fixed at the base. Faltinsen (1974), Faltinsen and Timokha (2002), and Frandsen and Borthwick (2003) presented approximate theoretical forms for inviscid sloshing motion in fixed and moving containers. Extensive numerical analyses of liquid slosh dynamics have been undertaken by using numerical methods such as the finite difference method, boundary element method, finite volume method, etc. Techniques, such as marker and cell (MAC), volume of fluid (VOF) are available to handle the free surface of the moving fluid (Popov *et al.*, 1993; Akyildiz and Unal, 2006; Cho *et al.*, 2005; Arafa, 2007; Hirt and Nichols, 1981; Eswaran *et al.*, 2009). Since these methods require complex computer programming to treat the time varying free surface boundary and computational mesh needs to be updated at every time step, use of σ -transformation for treating the liquid free surface has gained widespread popularity in recent years. The σ -transformation technique is simple, easy to implement and

Received date: 2012-10-14.

Accepted date: 2012-11-02.

*Corresponding author Email: saha@iitg.ac.in

© Harbin Engineering University and Springer-Verlag Berlin Heidelberg 2013

eliminates the need for remeshing of the computational domain at each time step. This technique was applied and found to produce good quality results by Chern *et al.* (1999), Turnbull *et al.* (2003), Chen and Nokes (2005), Dai and Xu (2006), Eswaran and Saha (2009a, 2009b, 2010). Originally, σ -transformation was proposed for meteorological weather forecasting by Phillips (1957), however, later, Blumberg and Mellor (1980) and Mellor and Blumberg (1985) applied it in the context of oceanic and coastal flows. Recently, Frandsen (2004) investigated numerically steep free surface sloshing in 2D fixed and base-excited rectangular containers, with a focus on moving liquid free surface using σ -transformation and compared the results with third-order single modal solutions and theoretical results (multidimensional modal analysis) of Faltinsen *et al.* (2000). Thus, it was revealed that all the investigations as reported above have used sigma transformation technique for 2D containers only. Studies addressing 3D containers have not been reported so far in literature reviews. In view of this, the current investigation, attempted to make simulated the 3D sloshing waves in a regularly and randomly excited container using σ -transformation technique. In order to achieve this, few modifications have also been performed in the existing σ -transformation technique.

The main objective of this paper was to develop a new computational algorithm for capturing the liquid free surface for idealized 2D and 3D sloshing waves of inviscid fluid in a rectangular liquid container. In order to accomplish this, a modified σ -transformation technique was used to map the asymmetric physical domain onto a square computational domain, such that the moving free surface in the physical plane becomes a fixed plane surface in the computational domain. The finite difference scheme was used to solve the discretized governing equations in the transformed computational domain to obtain the free surface elevation time histories, phase plane diagram, spectrum analysis and free surface profiles in the physical domain. The free surface elevations are captured in the regularly and randomly excited container in vertical direction at different locations of the 2D and 3D domains while varying the modes of oscillation ($n=1, 2$ and 3). Two initial wave profiles for the liquid free surface (i.e., initial profile 1, and initial profile 1 and 2, which is the result of linear superposition of two sinusoidal wave profiles) are used for the 3D fluid domain to observe the variation in the free surface elevation time histories at different locations of the container. Section 2 is focused on the mathematical formulation of the present work. Section 3 presents the mapping procedure which maps the physical domain onto the computational domain for 2D domain and 3D domain. In section 4, the finite difference discretizations of the governing equation and boundary conditions in the computational domain have been given. The free surface elevation of liquid, phase plane diagram, spectrum analysis and free surface profiles are discussed for vertically excited container in section 5.

2 Mathematical formulation

A rectangular Cartesian coordinate system was initially employed with origin on the mean free-surface at the left wall of the container. Primarily, a 2D nonlinear wave problem was considered, as depicted in Fig. 1, where ζ is the free-surface elevation above still water level, b is the length of the container, and h_s is the still water depth. The fluid in the container was assumed to be inviscid and irrotational. Taking the assumption that the fluid was governed by potential flow theory, the velocity potential ϕ satisfies the Laplace equation. The velocity components normal to the fixed boundaries were zero by definition. The left, right and bottom boundaries were indicated by L, R, and B, respectively (Fig. 1). The free surface occurs at the interface between two fluids. Such an interface requires two boundary conditions to be applied, viz., (i) a kinematic condition that relates the motion of the free interface to the fluid velocities at the free surface (i.e., T_1) and (ii) a dynamic condition which is concerned with the force balance at the free surface (i.e., T_2). Liquid velocity components normal to the walls and bottom of the container were zero. Zero pressure at the free surface of the fluid was also assumed for the analysis. In view of the fact mentioned above, kinematic and dynamic conditions must be satisfied on the free surface. Therefore, the governing equations in the physical domain were presented as,

$$\frac{\partial^2 \phi}{\partial x^2} + \frac{\partial^2 \phi}{\partial y^2} = 0 \quad \text{in the fluid domain} \quad (1)$$

$$\frac{\partial \phi}{\partial n} = 0 \quad \text{on the side wall} \quad (2)$$

$$\frac{\partial \zeta}{\partial t} + \frac{\partial \phi}{\partial x} \frac{\partial \zeta}{\partial x} = \frac{\partial \phi}{\partial y} \quad \text{on the free surface} \quad (3)$$

$$\frac{\partial \phi}{\partial t} + \frac{1}{2} \nabla \phi \cdot \nabla \phi + (g + \ddot{Y}_t) \zeta = 0 \quad \text{on the free surface} \quad (4)$$

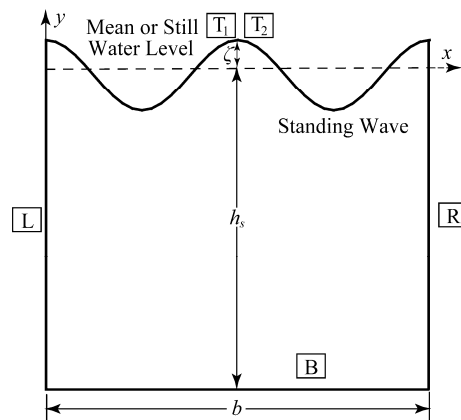


Fig. 1 Sketch of a standing wave in 2D container

Here, \ddot{Y}_t is the acceleration of the container in the vertical direction which can be neglected from the free surface dynamic boundary condition for fixed container

analysis. The following quantities were introduced for generating dimensionless governing equations for the present study,

$$x' = \frac{x}{b}; y' = \frac{y}{b}; \zeta' = \frac{\zeta}{A}; \ddot{Y}_t' = \frac{\ddot{Y}_t}{g}; t' = \sqrt{\frac{g}{b}} t; \phi' = \frac{1}{A\sqrt{bg}} \phi \quad (5)$$

where g is the acceleration due to gravity, A the wave amplitude, \ddot{Y}_t the acceleration of the container and t the time. Here x' , y' , ζ' , \ddot{Y}_t' , t' and ϕ' represent the dimensionless quantities. Using Eq. (5) (hereafter, primes are omitted for simplification), the non-dimensional governing equation and boundary conditions can be written as following,

$$\frac{\partial^2 \phi}{\partial x^2} + \frac{\partial^2 \phi}{\partial y^2} = 0 \quad (6)$$

$$L: \frac{\partial \phi}{\partial x} = 0 \quad \text{on} \quad x = 0 \quad (7)$$

$$R: \frac{\partial \phi}{\partial x} = 0 \quad \text{on} \quad x = b \quad (8)$$

$$B: \frac{\partial \phi}{\partial y} = 0 \quad \text{on} \quad y = -h_s \quad (9)$$

$$T_1: \frac{\partial \zeta}{\partial t} + E_b \frac{\partial \phi}{\partial x} \frac{\partial \zeta}{\partial x} = \frac{\partial \phi}{\partial y} \quad \text{on} \quad y = \zeta \quad (10)$$

$$T_2: \frac{\partial \phi}{\partial t} + E_b \frac{1}{2} \nabla \phi \cdot \nabla \phi + (1 + \ddot{Y}_t') \zeta = 0 \quad \text{on} \quad y = \zeta \quad (11)$$

where $E_b = A/b$ is the amplitude-length ratio. The Eqs. (6) through (11) form an initial boundary value problem which is the Laplace equation with non-linear boundary conditions imposed on the free surface. Here, the non-linearity was significant for two reasons. Primarily, the elevation of the moving free surface was not known a priori or at any given time instant and, the boundary conditions on the free surface (i.e., Eqs. (10) and (11)) contain second order differential terms or products of unknown parameters.

3 Mapping procedure

The time-varying liquid free surface can be mapped onto a fixed plane surface by the proper coordinate transformations, called the σ -transformation, which prevents the need for free surface smoothing for the cases considered herein. In this paper, σ -transformation applied in the horizontal direction which stretches between the left and the right wall and in the vertical direction which stretches between the moving liquid free surface and the bottom of the liquid container to convert the moving free-surface physical domain onto a fixed square computational domain. The following section discusses the transformation technique in 2D and 3D containers in detail. During the transformation, the corresponding governing equation and boundary conditions will change appropriately.

3.1 Transformation of 2D container

Initially, formulations were developed for the fixed

container condition, so the horizontal and vertical excitation terms were neglected from the Eq. (4) in the following formulation part.

Step 1: First coordinate transformation

The first transformation adopted the σ -transformation technique to map the liquid domain onto a rectangle, such that the moving free surface in the physical plane (Fig. 2) becomes a fixed horizontal line in the σ -transformed domain (Fig. 3). The mapping function $\sigma(x, t)$ was defined as

$$\sigma = \frac{y + h_s}{h} \quad (12)$$

where

$$h(x, t) = E_b \zeta(x, t) + h_s \quad (13)$$

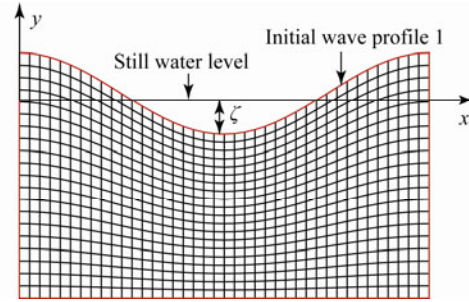


Fig. 2 The 2D physical domain

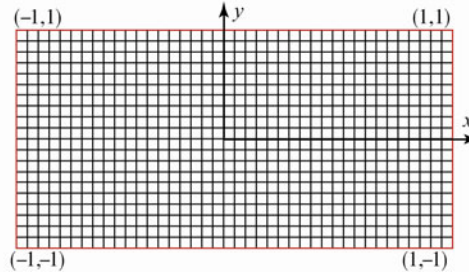


Fig. 3 The 2D intermediate domain after first transformation

Here, $\sigma(x, t)$ is the stretching factor, which varies from 0 to 1. The value of σ at the bottom of the container is 0, while at the free surface is 1. The first-order derivatives of σ can be calculated as follows:

$$\begin{aligned} \frac{\partial \sigma}{\partial t} &= \frac{\partial}{\partial t} \left(\frac{y + h_s}{h} \right) = -E_b \frac{\sigma}{h} \frac{\partial \zeta}{\partial t} \\ \frac{\partial \sigma}{\partial x} &= -E_b \frac{\sigma}{h} \frac{\partial \zeta}{\partial x} \end{aligned} \quad (14)$$

The potential function $\phi(x, y, t)$ in the physical domain was transformed to the potential function $\Phi(X, \sigma, T)$ in the σ -transformed domain.

$$\begin{aligned} x &\leftrightarrow X, \quad X = 2x - 1 \\ y &\leftrightarrow Y, \quad Y = 2\sigma - 1 \\ t &\leftrightarrow T, \quad T = t \end{aligned} \quad (15)$$

Using the chain rule, the first set of derivatives of ϕ with respect to x, y and t gets transformed as

$$\frac{\partial \phi}{\partial x} = 2 \frac{\partial \Phi}{\partial X} - E_b \frac{4\sigma}{h} \frac{\partial \zeta}{\partial X} \frac{\partial \Phi}{\partial Y} \quad (16)$$

$$\frac{\partial \phi}{\partial y} = \frac{2}{h} \frac{\partial \Phi}{\partial Y} \quad (17)$$

$$\frac{\partial \phi}{\partial t} = \frac{\partial \Phi}{\partial T} - E_b \frac{\sigma}{h} \frac{\partial \zeta}{\partial T} \frac{\partial \Phi}{\partial \sigma} \quad (18)$$

The second set of derivatives of ϕ with respect to x and y gets transformed as,

$$\frac{\partial^2 \phi}{\partial x^2} = 4 \frac{\partial^2 \Phi}{\partial X^2} + l_1 \frac{\partial^2 \Phi}{\partial Y^2} - l_2 \frac{\partial^2 \Phi}{\partial X \partial Y} + l_3 \frac{\partial \Phi}{\partial Y} \quad (19)$$

$$\frac{\partial^2 \phi}{\partial y^2} = \frac{4}{h^2} \frac{\partial^2 \Phi}{\partial Y^2} \quad (20)$$

where $l_1 = \left(\frac{4\sigma}{h} \frac{\partial h}{\partial X} \right)^2$, $l_2 = \left[\frac{8\sigma}{h} \frac{\partial h}{\partial X} \right]$, $l_3 = \left[\sigma \left(\frac{4}{h} \frac{\partial h}{\partial X} \right)^2 - \frac{8\sigma}{h} \frac{\partial^2 h}{\partial X^2} \right]$.

Hence, by using the σ -transformation, we can derive the new governing equation and boundary conditions specified on the rectangular σ -transformed domain. The governing equation after the first coordinate transformation was provided as:

$$\frac{\partial^2 \Phi}{\partial X^2} + L_1 \frac{\partial \Phi}{\partial Y} - L_2 \frac{\partial^2 \Phi}{\partial X \partial Y} + L_3 \frac{\partial^2 \Phi}{\partial Y^2} = 0 \quad (21)$$

where

$$L_1 = \left[\frac{4\sigma}{h^2} \left(\frac{\partial h}{\partial X} \right)^2 - \frac{2\sigma}{h} \frac{\partial^2 h}{\partial X^2} \right]$$

$$L_2 = 2 \frac{\sigma}{h} \frac{\partial h}{\partial X} \quad (22)$$

$$L_3 = \left[\frac{1}{h^2} + \left(\frac{2\sigma}{h} \frac{\partial h}{\partial X} \right)^2 \right]$$

Boundary conditions after the first coordinate transformation are given as:

$$\text{L: } \frac{\partial \Phi}{\partial X} - \frac{2\sigma}{h} \frac{\partial h}{\partial X} \frac{\partial \Phi}{\partial Y} = 0 \quad \text{on } X = -1 \quad (23)$$

$$\text{R: } \frac{\partial \Phi}{\partial X} - \frac{2\sigma}{h} \frac{\partial h}{\partial X} \frac{\partial \Phi}{\partial Y} = 0 \quad \text{on } X = +1 \quad (24)$$

$$\text{B: } \frac{\partial \Phi}{\partial Y} = 0, \quad \text{on } Y = -1 \quad (25)$$

$$\text{T}_1: \frac{\partial \zeta}{\partial T} = \left[\frac{2}{h} + \frac{8E_b \sigma}{h} \left(\frac{\partial \zeta}{\partial X} \right)^2 \right] \frac{\partial \Phi}{\partial Y} - 4E_b \frac{\partial \Phi}{\partial X} \frac{\partial \zeta}{\partial X}, \quad \text{on } Y = +1 \quad (26)$$

$$\text{T}_2: \frac{\partial \Phi}{\partial T} = M_1 \frac{\partial \Phi}{\partial Y} - 2E_b \left[\left(\frac{\partial \Phi}{\partial X} - M_2 \frac{\partial \Phi}{\partial Y} \right)^2 + \left(\frac{1}{h} \frac{\partial \Phi}{\partial Y} \right)^2 \right] - \quad (27)$$

$$(1 + \ddot{Y}_t) \zeta, \quad \text{on } Y = +1$$

where

$$M_1 = \frac{2\sigma}{h} \frac{\partial h}{\partial T}; \quad M_2 = \frac{2\sigma}{h} \frac{\partial h}{\partial X} \quad (28)$$

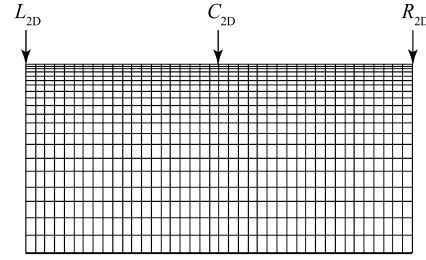


Fig. 4 The 2D computational domain after second transformation

Step 2: Second coordinate transformation

After the first coordinate transformation, the liquid domain becomes a rectangle defined by $-1 \leq X \leq +1$, $-1 \leq Y \leq +1$. The time-varying curved free surface was, hence, replaced by the fixed straight line. Any numerical method can be employed to solve the governing equations in the computational domain. Now the second transformation was performed for the clustering of grid points near liquid free surface. The second coordinate transformation was applied by the following equations

$$\begin{aligned} X &\leftrightarrow \xi, \quad \xi = X \\ Y &\leftrightarrow \eta, \quad \eta = \alpha + (1-\alpha) \frac{\ln \left[\left(\beta + \left[\frac{Y+1}{h_{cd}} \right] \right) / \left(\beta - \left[\frac{Y+1}{h_{cd}} \right] \right) \right]}{\ln(\beta+1/\beta-1)} \\ T &\leftrightarrow \tau, \quad \tau = T \end{aligned} \quad (29)$$

where β is the grid vertical stretching factor and α is a parameter that controls the range of η . The above transformation produces clustering of the grids near the free surface depending on the value of β selected. The clustering of grids near the free surface improved accuracy and eased convergence of the computational algorithm. As β approaches unity, the mesh gets increasingly refined along the free surface of the liquid. Another parameter in the transformation α adjusts the position of the bottom in the transformed coordinates. Here the value of α has been taken as -1 so that the computational domain after the second transformation is a rectangle defined by $-1 \leq \xi \leq 1$ and $-1 \leq \eta \leq 1$ with grid stretching near free surface as shown in Fig. 4. The mapping was performed from the σ -transformed $\Phi(X, Y, T)$ domain to the computational domain $\varphi(\xi, \eta, \tau)$. $h(X, T)$, the height of the liquid surface was transformed to $h_*(\xi, \tau)$, the height of the liquid surface in the transformed computational domain. h_{cd} was the difference between the nodal indices along Y axis of the grid after the first coordinate transformation.

The derivatives of the function $\Phi(X, Y, T)$ with respect to X , Y and T were transformed into derivatives of $\varphi(\xi, \eta, \tau)$ with respect to ξ , η and τ . The first set of derivatives of $\Phi(X, Y, T)$ gets transformed as:

$$\frac{\partial \Phi}{\partial X} = \frac{\partial \varphi}{\partial \xi}, \quad \frac{\partial \Phi}{\partial Y} = \frac{\partial \varphi}{\partial \eta} \times \frac{\partial \eta}{\partial Y}, \quad \frac{\partial \Phi}{\partial T} = \frac{\partial \varphi}{\partial \tau} \quad (30)$$

where

$$\frac{\partial \eta}{\partial Y} = \frac{(1-\alpha)}{\ln(\beta+1/\beta-1)} \times \frac{2\beta}{h_{cd} \times (\beta^2 - \sigma^{*2})} \quad (31)$$

The second set of derivatives gets transformed as follows:

$$\frac{\partial^2 \Phi}{\partial X^2} = \frac{\partial^2 \varphi}{\partial \xi^2}, \quad \frac{\partial^2 \Phi}{\partial X \partial Y} = \frac{\partial^2 \varphi}{\partial \xi \partial \eta} \times \frac{\partial \eta}{\partial Y}, \quad \frac{\partial^2 \Phi}{\partial Y^2} = \frac{\partial^2 \varphi}{\partial \eta^2} \times \left(\frac{\partial \eta}{\partial Y} \right)^2 + \frac{\partial \varphi}{\partial \eta} \times C_1 \quad (32)$$

After the second coordinate transformation the governing equation (Eq. 12) becomes,

$$\frac{\partial^2 \varphi}{\partial \xi^2} + L_1 \frac{\partial \varphi}{\partial \eta} - C_3 L_2 \frac{\partial^2 \varphi}{\partial \xi \partial \eta} + C_3^2 L_3 \frac{\partial^2 \varphi}{\partial \eta^2} = 0 \quad (33)$$

where

$$\begin{aligned} L_1 &= \left(\frac{4\sigma^*}{h_*^2} \left[\frac{\partial h_*}{\partial \xi} \right]^2 - \frac{2\sigma^*}{h_*} \frac{\partial^2 h_*}{\partial \xi^2} + C_1 \times L_3 \right) \\ L_2 &= \left[\frac{2\sigma^*}{h_*} \frac{\partial h_*}{\partial \xi} \right] \\ L_3 &= \left[\frac{1}{h_*^2} + L_2^2 \right] \\ C_1 &= \frac{(1-\alpha)}{\ln(\beta+1)/(\beta-1)} \times \frac{4 \times \beta \times \sigma^* \times C_2}{\left(h_{cd} \times (\beta^2 - \sigma^{*2}) \right)^2} \\ C_2 &= \frac{\beta \times \left[(\beta-1)^{\frac{\eta-\alpha}{1-\alpha}} - (\beta+1)^{\frac{\eta-\alpha}{1-\alpha}} \right] \times C_5}{\left[(\beta+1)^{\frac{\eta-\alpha}{1-\alpha}} + (\beta-1)^{\frac{\eta-\alpha}{1-\alpha}} \right]^2} + \frac{\beta \times C_4}{(\beta+1)^{\frac{\eta-\alpha}{1-\alpha}} + (\beta-1)^{\frac{\eta-\alpha}{1-\alpha}}} \\ C_3 &= \frac{\partial \eta}{\partial Y} \\ C_4 &= \left(\frac{\log(\beta-1)(\beta-1)^{\frac{\eta-\alpha}{1-\alpha}}}{(\alpha-1)} - \frac{\log(\beta+1)(\beta+1)^{\frac{\eta-\alpha}{1-\alpha}}}{(\alpha-1)} \right) \\ C_5 &= \left(\frac{\log(\beta-1)(\beta-1)^{\frac{\eta-\alpha}{1-\alpha}}}{(\alpha-1)} + \frac{\log(\beta+1)(\beta+1)^{\frac{\eta-\alpha}{1-\alpha}}}{(\alpha-1)} \right) \\ \sigma^* &= \left(\beta \times \left[\frac{(\beta+1)^{\frac{\eta-\alpha}{1-\alpha}} - (\beta-1)^{\frac{\eta-\alpha}{1-\alpha}}}{(\beta+1)^{\frac{\eta-\alpha}{1-\alpha}} + (\beta-1)^{\frac{\eta-\alpha}{1-\alpha}}} \right] \right) \end{aligned} \quad (34)$$

Boundary conditions after the second transformation were given as:

$$\text{L:} \quad \frac{\partial \varphi}{\partial \xi} - \frac{2\sigma^*}{h_*} C_3 \frac{\partial h_*}{\partial \xi} \frac{\partial \varphi}{\partial \eta} = 0 \quad \text{on} \quad \xi = -1 \quad (35)$$

$$\text{R:} \quad \frac{\partial \varphi}{\partial \xi} - \frac{2\sigma^*}{h_*} C_3 \frac{\partial h_*}{\partial \xi} \frac{\partial \varphi}{\partial \eta} = 0 \quad \text{on} \quad \xi = 1 \quad (36)$$

$$\text{B:} \quad \frac{\partial \varphi}{\partial \eta} = 0 \quad \text{on} \quad \eta = -1 \quad (37)$$

$$\text{T}_1: \quad \frac{\partial \zeta^*}{\partial \tau} = L_4 C_3 \frac{\partial \varphi}{\partial \eta} - 4E_b \frac{\partial \varphi}{\partial \xi} \frac{\partial \zeta}{\partial \xi} \quad \text{on} \quad \eta = 1 \quad (38)$$

$$\begin{aligned} \text{T}_2: \quad \frac{\partial \varphi}{\partial \tau} &= -2E_b \left[\left(\frac{\partial \varphi}{\partial \xi} - C_3 L_6 \frac{\partial \varphi}{\partial \eta} \right)^2 + \left(\frac{C_3}{h_*} \frac{\partial \varphi}{\partial \eta} \right)^2 \right] + \\ &C_3 L_5 \frac{\partial \varphi}{\partial \eta} - (1 + Y_r^*) \zeta^* \quad \text{on} \quad \eta = 1 \end{aligned} \quad (39)$$

where

$$L_4 = \left[\frac{2}{h_*} + 4E_b L_2 \left(\frac{\partial h_*}{\partial \xi} \right) \right]; \quad L_5 = \frac{2\sigma^*}{h_*} \frac{\partial h_*}{\partial \tau}; \quad L_6 = \left[\frac{2\sigma^*}{h_*} \frac{\partial h_*}{\partial \xi} \right] \quad (40)$$

The governing equation and the boundary conditions in the computational domain were provided by Eqs. (33)–(40) and any numerical method can be used to solve them. One more feature of this σ -transformation technique was that it could easily be extended to 3D coordinates in a similar way.

3.2 Extension to 3D rectangular container

The 3D rectangular domain was bounded by 5 regular surfaces and 1 free surface. The velocity components normal to the fixed surfaces were zero. The left, right, front and back and the bottom boundary conditions were indicated by LB, RB, FB, BB and BMB, respectively in Eqs. (42)–(44). As usual, the top surface had two boundary conditions, viz. the kinematic condition (TB₁) and dynamic condition (TB₂). When the container was subjected to vertical acceleration, the non-dimensional governing equations based on the potential flow theory are as follows:

$$\frac{\partial^2 \phi}{\partial x^2} + \frac{\partial^2 \phi}{\partial y^2} + \frac{\partial^2 \phi}{\partial z^2} = 0 \quad (41)$$

$$\text{LB and RB:} \quad \frac{\partial \phi}{\partial x} = 0 \quad \text{on} \quad x = 0, b \quad (42)$$

$$\text{FB and BB:} \quad \frac{\partial \phi}{\partial z} = 0 \quad \text{on} \quad z = 0, w \quad (43)$$

$$\text{BMB:} \quad \frac{\partial \phi}{\partial y} = 0 \quad \text{on} \quad y = -h_s \quad (44)$$

$$\text{TB}_1: \quad \frac{\partial \zeta}{\partial t} + E_b \frac{\partial \phi}{\partial x} \frac{\partial \zeta}{\partial x} + E_b \frac{\partial \phi}{\partial z} \frac{\partial \zeta}{\partial z} = \frac{\partial \phi}{\partial y} \quad \text{on} \quad y = \zeta \quad (45)$$

$$\text{TB}_2: \quad \frac{\partial \phi}{\partial t} + E_b \frac{1}{2} \nabla \phi \cdot \nabla \phi + (1 + \ddot{Y}_l) \zeta = 0 \quad \text{on} \quad y = \zeta \quad (46)$$

where w is width of the rectangular container. The derivation of the governing equations can be performed in the same way as the two-dimensional case by the following two transformations. The first transformation was performed for conversion from physical domains (Figs. 5 and 6) to σ -transformed domain (Fig. 7) and the second transformation was for σ -transformed domain to computational domain (Fig. 8).

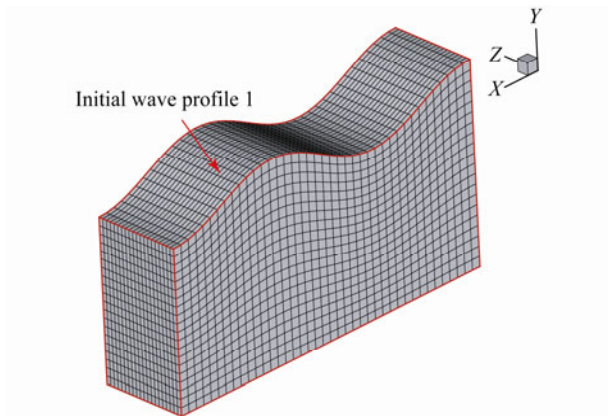


Fig. 5 The 3D physical domain with initial wave profile 1

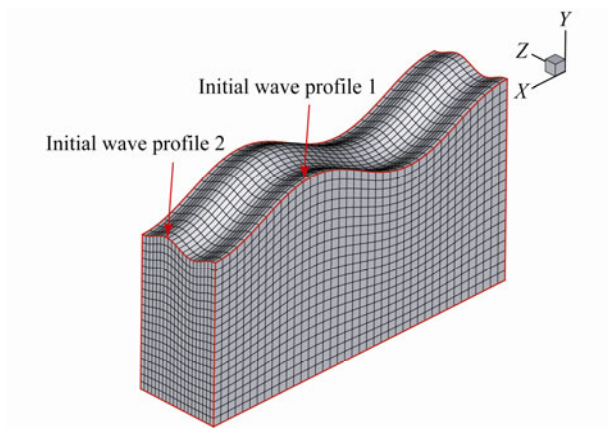


Fig. 6 The 3D physical domain with initial wave profile 1 and 2

The mapping relations for first transformation were provided as,

$$X = 2x - 1; Y = 2\sigma - 1; Z = 2z - 1; T = t \quad (47)$$

Hence the transformed governing equation becomes:

$$\frac{\partial^2 \Phi}{\partial X^2} + K_1 \frac{\partial \Phi}{\partial Y} - K_2 \frac{\partial^2 \Phi}{\partial X \partial Y} - K_3 \frac{\partial^2 \Phi}{\partial Z \partial Y} + K_4 \frac{\partial^2 \Phi}{\partial Y^2} + \frac{\partial^2 \Phi}{\partial Z^2} = 0 \quad (48)$$

where

$$K_1 = \left[\frac{4\sigma}{h^2} \left(\frac{\partial h}{\partial X} \right)^2 - \frac{2\sigma}{h} \frac{\partial^2 h}{\partial X^2} + \frac{4\sigma}{h^2} \left(\frac{\partial h}{\partial Z} \right)^2 - \frac{2\sigma}{h} \frac{\partial^2 h}{\partial Z^2} \right];$$

$$K_2 = \frac{2\sigma}{h} \frac{\partial h}{\partial X}; K_3 = \frac{2\sigma}{h} \frac{\partial h}{\partial Z}; K_4 = \left[\frac{1}{h^2} + K_2^2 + K_3^2 \right] \quad (49)$$

The boundary conditions are given as:

$$\text{LB and RB: } \frac{\partial \Phi}{\partial X} - \frac{2\sigma}{h} \frac{\partial h}{\partial X} \frac{\partial \Phi}{\partial Y} = 0 \quad \text{on } X = -1, +1 \quad (50)$$

$$\text{FB and BB: } \frac{\partial \Phi}{\partial Z} - \frac{2\sigma}{h} \frac{\partial h}{\partial Z} \frac{\partial \Phi}{\partial Y} = 0 \quad \text{on } Z = -1, +1 \quad (51)$$

$$\text{BMB: } \frac{\partial \Phi}{\partial Y} = 0, \quad \text{on } Y = -1 \quad (52)$$

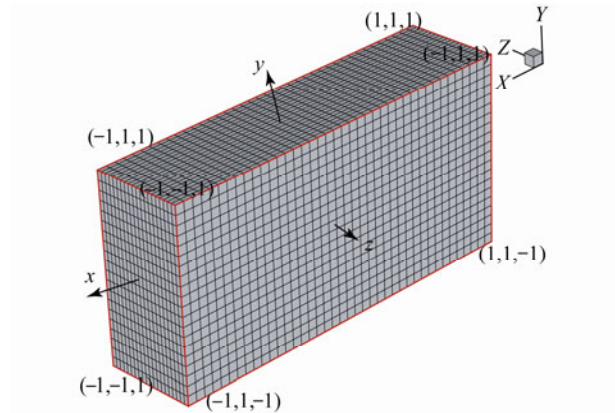


Fig. 7 The 3D intermediate domain after first transformation

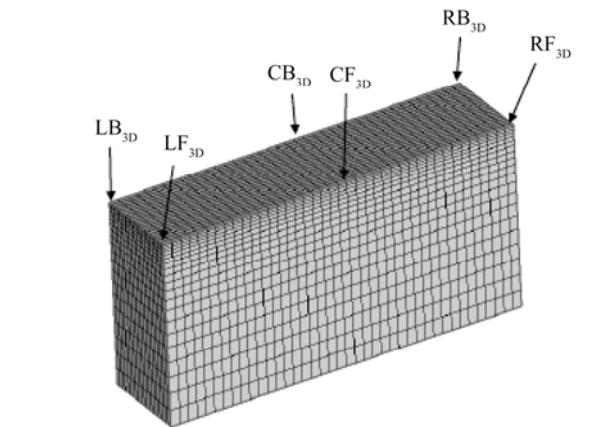


Fig. 8 The 3D intermediate domain after second transformation

On the free surface,

$$\text{TB}_1: \frac{\partial \zeta}{\partial T} = K_5 \frac{\partial \Phi}{\partial Y} - 4E_b \frac{\partial \Phi}{\partial X} \frac{\partial \zeta}{\partial X} - 4E_b \frac{\partial \Phi}{\partial Z} \frac{\partial \zeta}{\partial Z} \quad \text{on } Y = +1 \quad (53)$$

$$\text{TB}_2: \frac{\partial \Phi}{\partial T} = K_6 \frac{\partial \Phi}{\partial Y} - (1 + \ddot{Y}_t) \zeta +$$

$$2E_b \left[\left(\frac{\partial \Phi}{\partial X} - K_7 \frac{\partial \Phi}{\partial Y} \right)^2 + \left(\frac{1}{h} \frac{\partial \Phi}{\partial Y} \right)^2 + \left(\frac{\partial \Phi}{\partial Z} - K_8 \frac{\partial \Phi}{\partial Y} \right)^2 \right] \quad \text{on } Y = +1 \quad (54)$$

where

$$K_5 = \left[\frac{2}{h} + \frac{8E_b \sigma}{h} \left(\frac{\partial \zeta}{\partial X} \right)^2 + \frac{8E_b \sigma}{h} \left(\frac{\partial \zeta}{\partial Z} \right)^2 \right]; K_6 = \frac{2\sigma}{h} \frac{\partial h}{\partial T};$$

$$K_7 = \frac{2\sigma}{h} \frac{\partial h}{\partial X}; K_8 = \frac{2\sigma}{h} \frac{\partial h}{\partial Z} \quad (55)$$

The mapping relations for second transformation were given as,

$$X \leftrightarrow \xi, \xi = X; Z \leftrightarrow \kappa, \kappa = Z; T \leftrightarrow \tau, \tau = T;$$

$$Y \leftrightarrow \eta, \eta = \alpha + (1 - \alpha) \frac{\ln \left(\left(\beta + \left[\frac{Y+1}{h_{cd}} \right] \right) / \left(\beta - \left[\frac{Y+1}{h_{cd}} \right] \right) \right)}{\ln[(\beta+1)/(\beta-1)]} \quad (56)$$

The mapping was performed from the σ -transformed

$\Phi(X, Y, Z, T)$ domain to the computational domain $\varphi(\xi, \eta, \kappa, \tau)$. The height of the liquid, $h(X, Y, Z, T)$ surface was transformed to the height of the liquid in the transformed computational domain, $h_*(\xi, \kappa, \tau)$. The h_{cd} is the difference between the nodal indices along Y axis of the grid after the first coordinate transformation. The derivatives of the function $\Phi(X, Y, Z, T)$ with respect to X, Y, Z and T are transformed into derivatives of $\varphi(\xi, \eta, \kappa, \tau)$ with respect to ξ, η, κ and τ . After the second coordinate transformation the governing equation in the fluid domain becomes,

$$\frac{\partial^2 \varphi}{\partial \xi^2} + C_4 \frac{\partial \varphi}{\partial \eta} - C_3 U_1 \frac{\partial^2 \varphi}{\partial \xi \partial \eta} - C_3 U_2 \frac{\partial^2 \varphi}{\partial \kappa \partial \eta} + C_5 \frac{\partial^2 \varphi}{\partial \eta^2} = 0 \quad (57)$$

where $U_1 = \left[\frac{2\sigma^*}{h_*} \frac{\partial h_*}{\partial \xi} \right]; U_2 = \left[\frac{2\sigma^*}{h_*} \frac{\partial h_*}{\partial \kappa} \right]$

$$U_3 = \left(\frac{\log(\beta-1)(\beta-1)^{\frac{\eta-\alpha}{1-\alpha}}}{(\alpha-1)} - \frac{\log(\beta+1)(\beta+1)^{\frac{\eta-\alpha}{1-\alpha}}}{(\alpha-1)} \right)$$

$$U_4 = \left(\frac{\log(\beta-1)(\beta-1)^{\frac{\eta-\alpha}{1-\alpha}}}{(\alpha-1)} + \frac{\log(\beta+1)(\beta+1)^{\frac{\eta-\alpha}{1-\alpha}}}{(\alpha-1)} \right)$$

$$C_1 = \frac{(1-\alpha)}{\ln\left(\frac{\beta+1}{\beta-1}\right)} \times \frac{4\beta \times \sigma^* \times C_2}{\left(h_{cd} \times \left[\beta^2 - \sigma^{*2} \right]^2 \right)}$$

$$C_2 = \frac{\beta \times U_3}{(\beta+1)^{\frac{\eta-\alpha}{1-\alpha}} + (\beta-1)^{\frac{\eta-\alpha}{1-\alpha}}} + \frac{\beta \times \left[(\beta-1)^{\frac{\eta-\alpha}{1-\alpha}} - (\beta+1)^{\frac{\eta-\alpha}{1-\alpha}} \right] \times U_4}{\left[(\beta+1)^{\frac{\eta-\alpha}{1-\alpha}} + (\beta-1)^{\frac{\eta-\alpha}{1-\alpha}} \right]^2}$$

$$C_3 = \frac{\partial \eta}{\partial Y}$$

$$C_4 = \left(\frac{4\sigma^*}{h_*^2} \left[\left(\frac{\partial h_*}{\partial \xi} \right)^2 + \left(\frac{\partial h_*}{\partial \kappa} \right)^2 \right] \right) - \frac{2\sigma^*}{h_*} \left(\frac{\partial^2 h_*}{\partial \xi^2} + \frac{\partial^2 h_*}{\partial \kappa^2} \right) + C_1 \times U_5$$

$$U_5 = \left[\frac{1}{h_*^2} + \left(\frac{2\sigma^*}{h_*} \frac{\partial h_*}{\partial \xi} \right)^2 + \left(\frac{2\sigma^*}{h_*} \frac{\partial h_*}{\partial \kappa} \right)^2 \right]$$

$$C_5 = C_3^2 \times \left[\frac{1}{h_*^2} + \left(\frac{2\sigma^*}{h_*} \frac{\partial h_*}{\partial \xi} \right)^2 + \left(\frac{2\sigma^*}{h_*} \frac{\partial h_*}{\partial \kappa} \right)^2 \right]$$

$$\sigma^* = \left(\beta \left[\frac{(\beta+1)^{\frac{\eta-\alpha}{1-\alpha}} - (\beta-1)^{\frac{\eta-\alpha}{1-\alpha}}}{(\beta+1)^{\frac{\eta-\alpha}{1-\alpha}} + (\beta-1)^{\frac{\eta-\alpha}{1-\alpha}}} \right] \right) \quad (58)$$

Boundary conditions after the second transformation are given as:

$$\text{LB and RB: } \frac{\partial \varphi}{\partial \xi} - \frac{2\sigma^*}{h_*} C_3 \frac{\partial h_*}{\partial \xi} \frac{\partial \varphi}{\partial \eta} = 0 \quad \text{on } \xi = -1, 1 \quad (59)$$

$$\text{FB and BB: } \frac{\partial \varphi}{\partial \kappa} - \frac{2\sigma^*}{h_*} C_3 \frac{\partial h_*}{\partial \kappa} \frac{\partial \varphi}{\partial \eta} = 0 \quad \text{on } \kappa = -1, 1 \quad (60)$$

$$\text{BMB: } \frac{\partial \varphi}{\partial \eta} = 0 \quad \text{on } \eta = -1 \quad (61)$$

On the free surface,

$$T_1: \frac{\partial \zeta^*}{\partial \tau} = -4E_b \left(\frac{\partial \varphi}{\partial \xi} \frac{\partial \zeta^*}{\partial \xi} + \frac{\partial \varphi}{\partial \kappa} \frac{\partial \zeta^*}{\partial \kappa} \right) + C_3 \left[\frac{2}{h_*} + U_9 \right] \frac{\partial \varphi}{\partial \eta} \quad \text{on } \eta = 1 \quad (62)$$

$$T_2: \frac{\partial \varphi}{\partial \tau} = -2E_b \left[\left(\frac{\partial \varphi}{\partial \xi} - U_7 \frac{\partial \varphi}{\partial \eta} \right)^2 + \left(\frac{\partial \varphi}{\partial \kappa} - U_8 \frac{\partial \varphi}{\partial \eta} \right)^2 \right] - 2E_b \left(\frac{C_3}{h_*} \frac{\partial \varphi}{\partial \eta} \right)^2 + U_6 \frac{\partial \varphi}{\partial \eta} - (1 + Y_\tau^*) \zeta^* \quad \text{on } \eta = 1 \quad (63)$$

where

$$U_9 = \frac{8E_b \sigma^*}{h_*} \left(\left(\frac{\partial h_*}{\partial \xi} \right)^2 + \left(\frac{\partial h_*}{\partial \kappa} \right)^2 \right); U_7 = C_3 \frac{2\sigma^*}{h_*} \frac{\partial h_*}{\partial \xi};$$

$$U_8 = C_3 \frac{2\sigma^*}{h_*} \frac{\partial h_*}{\partial \kappa}; U_6 = C_3 \frac{2\sigma^*}{h_*} \frac{\partial h_*}{\partial \tau} \quad (64)$$

Since sloshing is a highly nonlinear phenomenon, the amplitude of excitation, frequency of excitation and container dimensions play a vital role in determining the shape of the nonlinear free surface. An amplitude–frequency relationship for the fluid response in a two-dimensional rectangular container was presented by Faltinsen *et al.* (2000). Obviously, the stretched grid system exactly matches the time-dependent free-surface wave profile due to the σ -transformation. Here, we should note that the mean water level in the container remains constant, so that the sum of the wave height along the x direction is kept at zero to maintain the volume conservation.

4 Finite difference discretization in the computational domain

In the current study, a finite difference scheme is used for the numerical study of the liquid sloshing. The computational domain is rectangular in shape for 2D numerical simulations and cuboidal for 3D numerical simulations. The governing equation and boundary conditions in the computational domain (Eqs. (33) to (40)) are discretized using finite difference method. Adams-Bashforth scheme is utilized for the computation of nonlinear solutions. As Adams-Bashforth scheme requires results from previous time steps to calculate the current time step result, hence the semi-implicit scheme is used to generate results for the initial time steps.

4.1 Semi-implicit scheme at top boundary (free surface)

The semi implicit scheme is applied at the top boundary of the computational domain. As discussed, the top boundary consists of two conditions, viz. kinematic condition and dynamic condition. In computational domain, the kinematic condition (Eq. (38)) was discretized by a forward scheme at $\eta = 1$ as follows

$$\left. \frac{\partial \zeta}{\partial \tau} \right|^n = L_4 C_3 \left. \frac{\partial \varphi}{\partial \eta} \right|^n - E_b \left. \frac{\partial \zeta}{\partial \xi} \right|^n \left. \frac{\partial \varphi}{\partial \xi} \right|^n \quad (65)$$

where

$$\left[\frac{\partial \zeta}{\partial T} \right]^n = \frac{\zeta^{n+1} - \zeta^n}{\Delta T} \quad (66)$$

At $\sigma = 1$, the dynamic condition (Eq. (39)) was discretized as:

$$\begin{aligned} \left. \frac{\partial \varphi}{\partial \tau} \right|^n &= C_3 L_5 \left. \frac{\partial \varphi}{\partial \eta} \right|^n - (1 + Y_\tau^*) \left. \zeta^* \right|^{n+1} - \\ &2E_b \left[\left(\left. \frac{\partial \varphi}{\partial \xi} \right|^n - C_3 L_6 \left. \frac{\partial \varphi}{\partial \eta} \right|^n \right)^2 + \left(\frac{C_3}{h_*^2} \left. \frac{\partial \varphi}{\partial \eta} \right|^n \right)^2 \right] \end{aligned} \quad (67)$$

where

$$\left[\frac{\partial \varphi}{\partial T} \right]^n = \frac{\varphi^{n+1} - \varphi^n}{\Delta T} \quad (68)$$

The value of ζ^{n+1} was computed using Eq. (66) and was substituted in Eq. (67). Then, the new φ^{n+1} was found at the top boundary of the computational domain using Eq. (68). The first and second order derivatives in above equations were discretized by means of second order central difference scheme within the liquid domain, and second order forward and backward differences were employed at the boundaries.

4.2 Adams-Bashforth scheme

The semi-implicit scheme was used to provide information at the first and second time steps, since the Adams-Bashforth was a multistep method. Euler and Runge-Kutta methods are single step methods, because they use only the information from the previous step. Adams methods are known as explicit schemes because current and previous time step values are used to obtain the values for future time steps. Here, three Point Adams-Bashforth schemes as mentioned in Eqs. (69) and (70) have been used.

$$(\Delta \varphi)^{n+1} = \frac{\Delta t}{12} (23\varphi^n - 16\varphi^{n-1} + 5\varphi^{n-2}) \quad (69)$$

$$(\varphi)^{n+1} = \varphi^n + (\Delta \varphi)^{n+1} + O(\Delta t^3) \quad (70)$$

The governing equation (Eq. (33)) was discretized by the standard fourth order central difference approximation and is given by

$$\delta_\xi^2 = \frac{-\varphi_{i-2,j} + 16\varphi_{i-1,j} - 30\varphi_{i,j} + 16\varphi_{i+1,j} - \varphi_{i+2,j}}{12(\Delta \xi^2)} + O(\xi^4) \quad (71)$$

$$\delta_\xi \delta_\eta = \frac{1}{2\Delta \xi} \left(\frac{\varphi_{i+1,j+1} - \varphi_{i+1,j-1}}{2(\Delta \eta)} - \frac{\varphi_{i-1,j+1} - \varphi_{i-1,j-1}}{2(\Delta \eta)} \right) + O(\xi^2, \eta^2) \quad (72)$$

where $\varphi(i, j)$ denotes $\varphi(\xi_i, \eta_j)$; δ_ξ, δ_ξ^2 and $\delta_\eta, \delta_\eta^2$ are the first and second order central difference operators along ξ and η directions respectively, and $\delta_\xi \delta_\eta$ is the mixed second order central difference operator.

4.3 Convergence criteria used for the iterative solver

It can be seen that the numerical algorithm requires solving a linear equation $A\phi = B$ in the fluid domain at every time step. To solve this equation various methods are available, but the iterative methods have been chosen for this work to find the solution to the velocity potential ϕ at every time step since these are known to have the advantages of lesser discretization error and better speed of computation as compared to other direct methods. Successive over relaxation method has been chosen to solve the linear equation. Using an iterative solver it is very important to stop the iterations at the right time, i.e., when the iteration error has decreased by an acceptable amount. Iteration errors (Ferziger and Peric, 2002) can be calculated as,

$$\delta^n = \phi^{n+1} - \phi^n \approx (\lambda_1 - 1)(\lambda_1)^n a_1 \psi_1 \quad (73)$$

where δ^n is the difference between solutions at iterations $n+1$ and n , and λ_1 is the spectral radius or the largest eigenvalue of the iteration matrix. It can be estimated from Eq. (74).

$$\lambda_1 \approx \frac{\|\delta^n\|}{\|\delta^{n-1}\|} \quad (74)$$

where $\|a\|$ represents the norm (here, chosen as root mean square) of a . After obtaining an estimate of the largest eigenvalue (λ_1), the iteration error can be approximated from Eq. (75).

$$\|\varepsilon^n\| = \phi - \phi^n \approx \frac{\|\delta^n\|}{\lambda_1 - 1} \quad (75)$$

Hence a good estimate of iteration error is available. The above given procedure produces pretty accurate results. The volume errors for all the cases studied were found to be within the range of $[-10^{-6}, 10^{-6}]$ as shown in Fig. 9. This procedure is better than the difference procedure used to stop the iterative solver (where the iterations are stopped when the difference between two successive iterations falls below a predefined tolerance limit) since the difference between two successive iterations falling below a particular limit does not ensure that the iteration error has also fallen down by the same order. Another widely used criterion for stopping is the residual stopping criterion, where the iterative solver is stopped when the residual norm falls below a preset fraction (tolerance limit) of its initial value. The residual and iteration error are related as,

$$A\varepsilon_n = \rho_n \quad (76)$$

where A represents the iteration matrix, ε_n the iteration error norm and ρ_n the residual norm at any particular iteration n . As we can notice from Eq. (67), that the residual is A times the iteration error, thus the reduction of the residual norm below the tolerance limit does not ensure that the error norm has also fallen below the same tolerance limit. Hence, it is essential for the iteration to have proper evaluation of error to ensure the accuracy of solutions. In the case of two dimensional vertical regular excitations in a rectangular container, a comparison was done for the various iterative solver stopping criteria as shown in Fig. 10. For iterations at the first time step, the variation of norm of the exact iteration error, estimated iteration error with the above procedure, residual and difference between two successive iterations was plotted against the iterations. It can be noted that the difference norm falls well below 0.1×10^{-5} by 50 iterations whereas the exact iteration error is still above 0.2×10^{-5} , hence this stopping criterion is not suited for the present case.

Looking at the residual norm we can see that it has a quite higher value than the exact iteration error for all iterations. Estimated iteration error was noticed to be nearly the same as the exact iteration error in this case (except for the initial iterations where it shows slight oscillations). Using residual stopping criterion ensures that the exact iteration error has fallen well below the tolerance limit but it results in higher computational time for the solver without achieving higher accuracy than the estimated iteration error stopping criterion. Comparisons made for later time steps also showed a similar behavior of the norms of the stopping criteria with iterations. Hence, the error estimation stopping criteria for the SOR solver is most suited for the current problem.

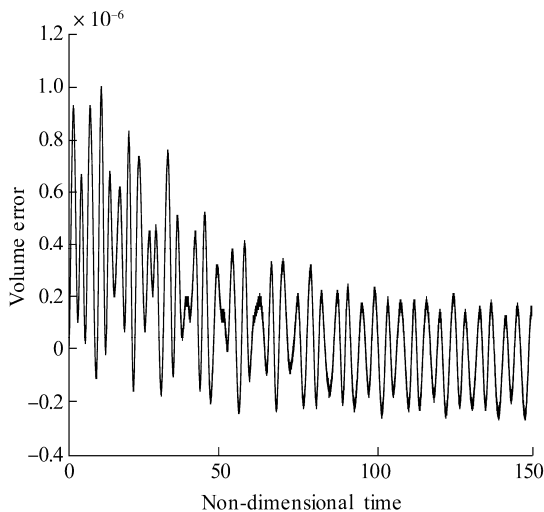


Fig. 9 Volume error for the 2D numerical simulation (for $n=1$, $\Omega_v = \frac{\omega_v}{\omega} = 1.253$, $K_v=0.4$, $E_b= 0.0033$ and $K_x=0.015$) versus non-dimensional time ($t \times \omega$)

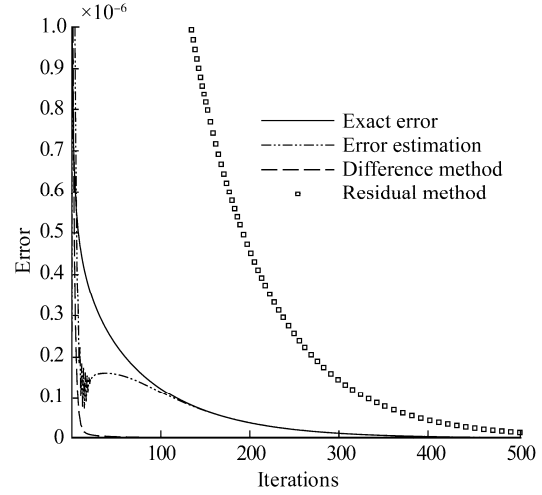


Fig. 10 Comparison of error norms for 2D container with 41×81 grid

5 Results and discussion

In the present study, the initial value of velocity potential (ϕ) is set to zero prescribed as, $\phi|_{t=0} = 0$, over the entire 2D liquid domain and the initial value of free surface elevation (ζ) is taken as $\zeta|_{t=0} = \zeta_0 = A \cos(K_n x)$. For 3D domain, initial value of free surface elevation (ζ) is considered in two cases say, initial profile 1 ($\zeta|_{t=0} = \zeta_0 = A \cos(K_n x)$) and initial profile 1 and 2 ($\zeta|_{t=0} = \zeta_0 = A \cos(K_n x) + A_v \cos(K_z z)$). Here, A and A_v are the respective amplitudes of the initial wave profiles on the liquid free surface along the X and Z axes (Fig. 6), $K_n (= \pi n/b)$, $K_z (= \pi n/w)$ are the respective wave numbers of the initial wave profiles on the liquid free surface along the X and Z axes for n th mode of oscillation ($n = 0, 1, 2, \dots$), and x and z are distances along the X and Z axes of the fluid container. The initial wave steepness defined for fixed container studies is as given below:

$$K_x = A \omega_n^2 / g \quad (77)$$

where A is the amplitude of the initial wave profile on the liquid free surface, ω_n the natural sloshing frequency of oscillations and g the acceleration due to gravity usually considered as 9.81 m/s^2 . Here, the ratio of h_s to b is considered as $1 : 2$. The linear natural sloshing frequencies in the two dimensional rectangular container is expressed as:

$$\omega_n = \sqrt{K_n g \tanh(K_n h_s)}, \quad n=1, 2, 3, \dots \quad (78)$$

Now the term \ddot{Y}_t in the dynamic boundary condition (Eq. (4)) was switched off for fixed container condition. Two quantities were of prime importance in the sloshing studies: the amplitude of the initial wave profile on the liquid free surface and the excitation frequency. Amplitude of the wave was determined from the wave steepness using Eq. (77). Here, numerical simulations are conducted for case A, case B,

case C, and case D. Case A represents 2D numerical simulation of regularly excited liquid container in vertical direction and case B represents 3D numerical simulation of regularly excited liquid container in vertical direction with initial profile 1 for liquid free surface. Case C represents 3D numerical simulation of regularly excited liquid container in vertical direction with initial profile 1 and 2 for fluid free surface and Case D represents the 3D numerical simulation of the randomly excited liquid container in vertical direction.

5.1 Grid independence and validation test

The wave characteristics include a crest at the top and a trough at the bottom. The difference in elevation between the crests and trough is the wave height. The distance between the adjacent crests or troughs of wave is termed as the wavelength. The ratio of wave height to wavelength is the wave's steepness. While increasing the wave steepness the nonlinearity of the wave increases. Before proceeding with the solution of the governing equations on the computational domain, grid independence study to choose a suitably refined grid for the solution is very important. Grid was successively refined along the three dimensional axes and the free surface plots along the container length for all the grids at time 7.5 seconds and $Z=0$ were compared. As shown in Fig. 11, initially the grid was refined in the horizontal and axial directions of container. Since the container was bounded by fixed vertical walls in the horizontal and axial directions, free surface plots do not seem to be affected by refining along these directions. But attention is required in the vertical direction, because of the moving free surface on the top. The grid points along the vertical direction were increased from 21 to 41 and then to 61 mesh points and we found that the free surface plot for the $41 \times 61 \times 41$ grid nearly overlaps with the free surface plot for the $41 \times 41 \times 41$ grid. Hence $41 \times 61 \times 41$ grid is a suitable grid for the current study.

Faltinsen *et al.* (2000) did comprehensive analysis of sloshing through theoretical and experimental techniques to provide results considered as benchmark results for the sloshing problems. Fig. 12 shows the comparison of present numerical work with theoretical result of Faltinsen *et al.* (2000) for the test case: $\omega_h = 1.283$; $A_h = 0.029$ m and $K_h = 0.069$. The wave peaks and troughs match well with present work. Therefore, the numerical solution was in reasonable agreement with the work of Faltinsen *et al.* (2000) for this particular test case. The specific test case was previously solved by Hill (2003) and Frandsen (2004) and similar results were obtained. Frandsen (2004) has compared his results with Faltinsen *et al.* (2000).

5.2 Vertically excited container: regular motion

The initial condition of the liquid free surface used to simulate sloshing in a vertically excited container is the same as for the sloshing motion simulation in a fixed container. It is difficult to simulate sloshing with a vertical excitation only. In order to have an initial perturbation in the free surface inside the container, horizontal motions need to be excited before the vertical excitation. To avoid this

situation, the initial standing wave profile was assumed for this work. Initial wave impulse at the fluid free surface was required for vertically excited condition and it is considered in two ways, initial profile 1 and initial profile 1 and 2 (as discussed in section 5). The vertical acceleration of the container is given by $\ddot{Y}_t = (-\omega_v A_v \cos(\omega_v t))$, where A_v is the vertical forcing amplitude, t is the time, ω_v is the angular frequency of forced vertical motion. The initial velocity potential in the fluid domain is considered as $\phi(\xi, \eta)|_{\tau=0} = 0$.

5.3 Effect of mode number on regular waves oscillation

The waves generated by the vertical excitation are called Faraday waves as explored by Faraday (1831) through his experiments. Faraday waves are the resonant waves when the excitation frequency is twice the natural frequency for some initial perturbation in the container. This resonance condition is called parametric resonance.

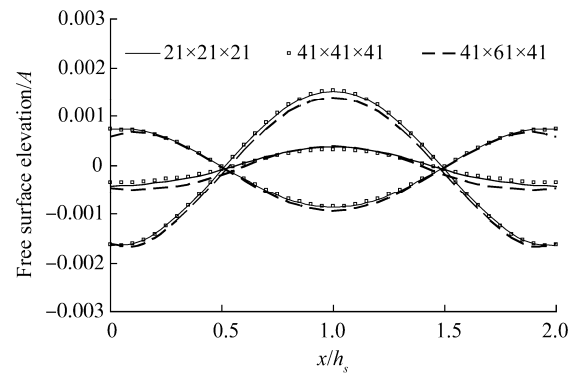


Fig. 11 Free surface plots along the container length for four different grids ($21 \times 21 \times 21$, $41 \times 21 \times 41$, $41 \times 41 \times 41$ and $41 \times 61 \times 41$) for $K_h=0.033$ at time 7.5 s and $Z=0$

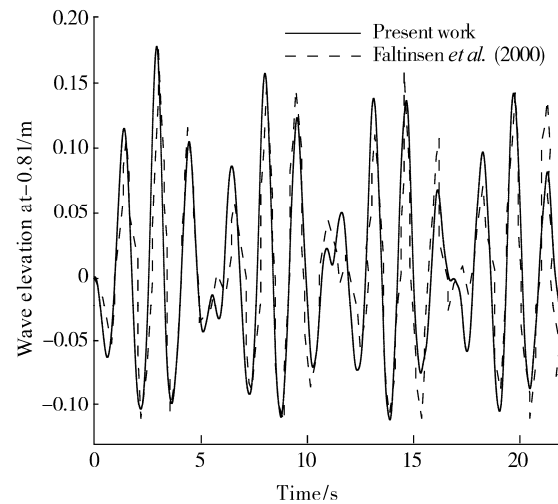


Fig. 12 Solution of Faltinsen *et al.* (2000) and the present work showing the free-surface elevation at the left wall in horizontally excited container; $\omega_h=1.283$, $A_h = 0.029$ m and $K_h = 0.069$

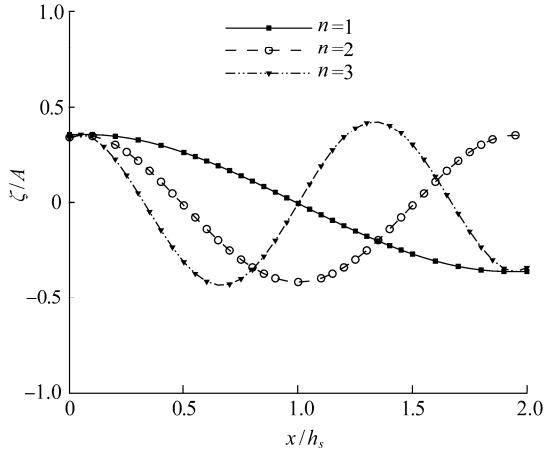


Fig. 13 Free surface profile diagram along container length at $t=1.5$ s

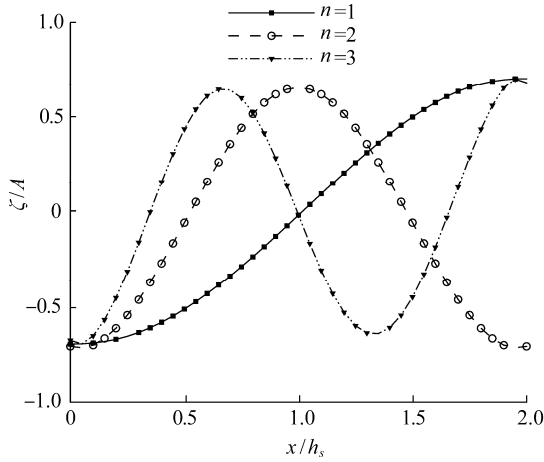


Fig. 14 Free surface profile diagram along container length at $t=3$ s

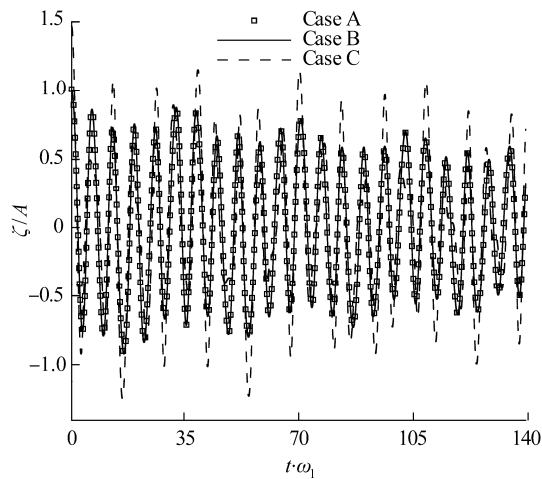


Fig. 15 Vertically excited container free surface wave elevation at left wall for $n=1$, $\Omega_v = \frac{\omega_v}{\omega} = 1.253$, $K_v = 0.4$, $E_b = 0.0033$ and $K_x = 0.015$

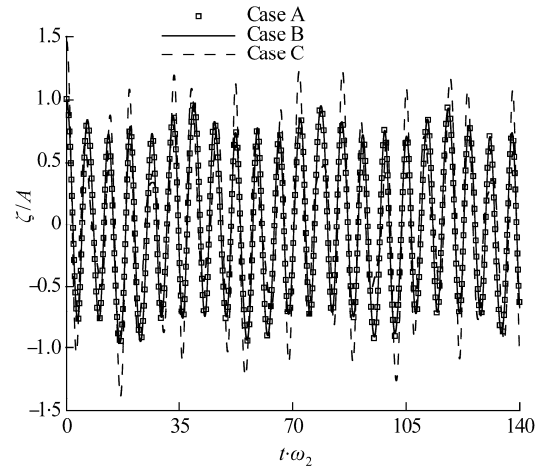


Fig. 16 Vertically excited container free surface wave elevation at left wall for $n=2$, $\Omega_v = \frac{\omega_v}{\omega} = 1.253$, $K_v = 0.4$, $E_b = 0.0024$ and $K_x = 0.015$

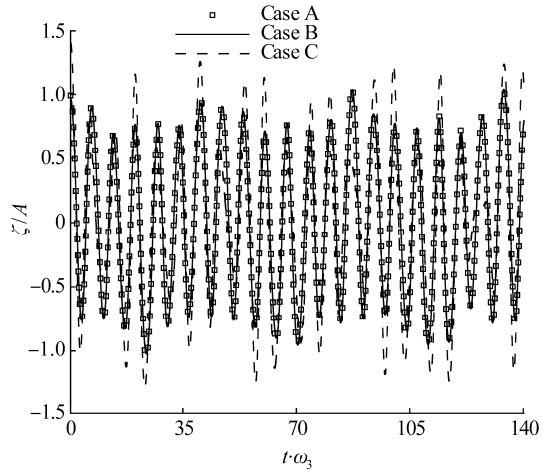


Fig. 17 Vertically excited container free surface wave elevation at left wall for $n=3$, $\Omega_v = \frac{\omega_v}{\omega} = 1.253$, $K_v = 0.4$, $E_b = 0.0016$ and $K_x = 0.015$

The study dealing with vertical excitation of liquid in a container was referred to as parametric sloshing. For the vertically excited container, the parameter $K_v = A_v \omega_v^2 / g$ is a measure of the importance of the vertical forcing motion and K_x (the wave steepness) is a measure of nonlinearity. Frandsen (2004) plotted the instability map between $\Omega_v = \omega_n / \omega_v$ and K_v and discussed results from stability and instability regions. If any of the pairs of the parameters lies in the instability region, then the corresponding mode grows exponentially with time. In this section, the profiles were given inside the stability region ($\Omega_v = 1.253$ and $K_v = 0.4$).

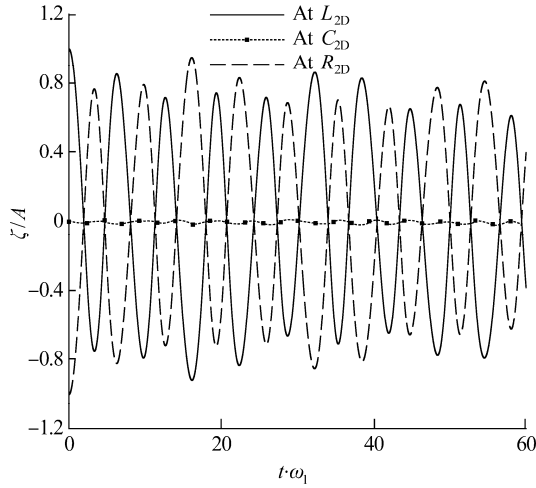


Fig. 18 Free surface elevation for case A at different locations (left wall (L), center (C) and right wall (R)) for $n=1$, $\Omega_v = \frac{\omega_v}{\omega} = 1.253$, $K_v=0.4$, $E_b=0.0033$ and $K_x=0.015$

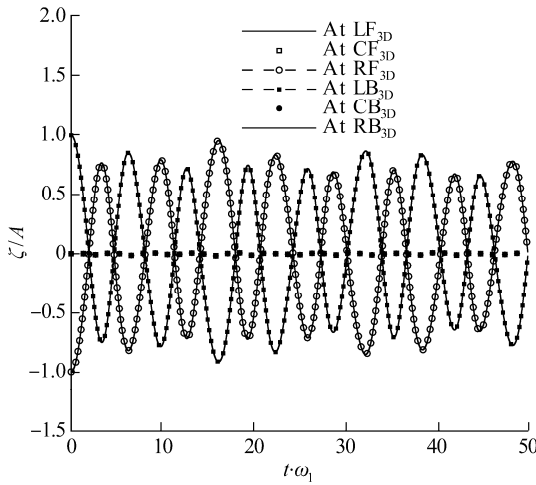


Fig. 19 Free surface elevation for case B with initial profile 1 at different locations (left front (LF), center front (CF), right front (RF), left back (LB), center back (CB) and right back (RB)) for $n=1$, $\Omega_v = \frac{\omega_v}{\omega} = 1.253$, $K_v=0.4$, $E_b=0.0033$ and $K_x=0.015$

Figs. 13 and 14 show liquid free surface elevation along the container length for $n=1, 2$ and 3 at time 1.5 and 3 seconds, respectively. The mode number defines the shape of the free surface during the numerical simulations. The first few mode natural frequencies of system are dangerous for the structural integrity of the container during violent motions.

Figs. 15 through 17 show the free surface elevations of the liquid near left wall (L_{2D} and LF_{3D}) for $n=1$, $\Omega_v=1.253$; $E_b=0.0033$ and $K_v=0.4$. The case A and case B show almost similar elevation histories. But, case C shows large wave oscillations.

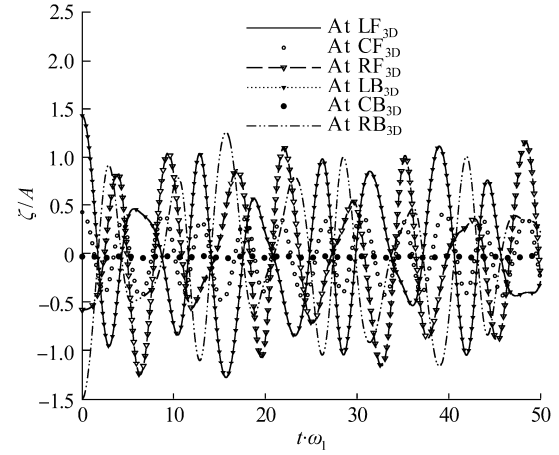


Fig. 20 Free surface elevation for case C at different locations (left front (LF), center front (CF), right front (RF), left back (LB), center back (CB) and right back (RB)) for $n=1$, $\Omega_v = \frac{\omega_v}{\omega} = 1.253$, $E_b=0.0033$, $K_v=0.4$; $K_x=0.015$

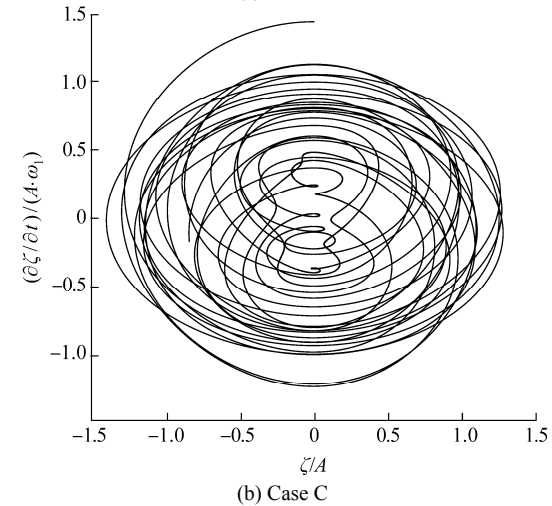
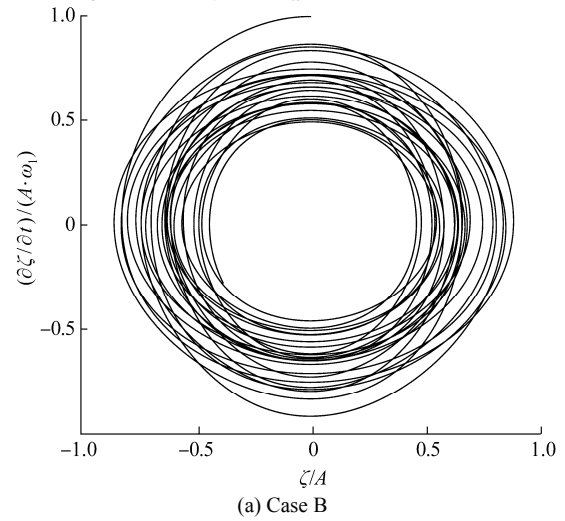


Fig. 21 Vertically excited container phase-plane diagram at LT_{3D} for $n=1$, $\Omega_v = \frac{\omega_v}{\omega} = 1.253$, $E_b=0.0033$, $K_v=0.4$, and $K_x=0.015$

5.4 Free surface elevation on different locations

Due to the wall effect, one can find the maximum wave amplitude near the wall, while the wave amplitude reduces as we move towards the centre. Here, three points were considered for case A (L_{2D} , C_{2D} and R_{2D}), and six points were considered for the case B and case C (LF_{3D} , CF_{3D} , RF_{3D} , LB_{3D} , CB_{3D} and RB_{3D}). These points were shown in Figs. 5 and 6. Fig. 18 shows free surface wave elevation time history in the vertically excited 2D container for case A at three different locations. The free surface wave elevation time history for case B and case C were shown in Figs. 19 and 20. In all cases, one can observe that the free surface elevation time histories of case A and case B are similar. Since the assumed initial profiles are the same in both cases (refer Fig. 2 and 3), the free surface wave elevation time histories are almost similar as well. But case C (3D with initial profile 1 and 2) shows dissimilar behavior and the difference between the crests and troughs also drastically varies from case B due to high nonlinearity. Fig. 21 (a) and (b) show the phase plane diagram at LT_{3D} for $\Omega_v = 1.253$, $E_b = 0.0033$ and $K_v = 0.4$. In Fig. 21 (a), the phase plane diagram shows the uniform repeating pattern, but Fig. 21(b) shows the non-uniform repeating pattern behavior.

5.5 Vertically excited container: random motion

In most practical situations, the excitation or the time variation of the system parameters were random in nature (Ibrahim, 2005). The behavior of such systems under deterministic or regular wave parametric excitation was an idealization and an oversimplification of the real behavior. The random excitation originates from many natural and artificial sources. Recently, the 2D sloshing waves generated by the random excitations were studied by Wang and Khoo (2005), and Sriram *et al.* (2006). The random vertical oscillation of the container was considered in this section. As we know, a random input wave can be generated by the linear superposition of a number of monochromatic waves. The total supplied energy to the system was kept constant. Bretschneider spectrum was selected to serve as the input excitation spectrum to generate the random input wave. The relation for the Bretschneider spectrum was as given in Eq. (79) and the spectrum and the corresponding displacement time history generated by the spectrum were shown in Figs. 22 and 23.

$$S_{\zeta}(\omega) = \frac{5H_s^2}{16\omega_p} \left(\frac{\omega_p}{\omega} \right)^5 \exp \left[-\frac{5}{4} \left(\frac{\omega_p}{\omega} \right)^4 \right] \quad (79)$$

where H_s is the significant wave height, and ω_p is the modal or peak frequency of the wave. The random input excitation wave is described by,

$$\zeta = \sum_{i=1}^{N_w} A_i \sin(\omega_i t + \psi_i) \quad (80)$$

where t is time, ω_i the frequency of i th linear wave, and N_w the number of the linear monochromatic waves. A_i and

ψ_i are the wave amplitude and phase of each linear wave, respectively. ω_i and ψ_i are a set of random variables within a pre-selected range.

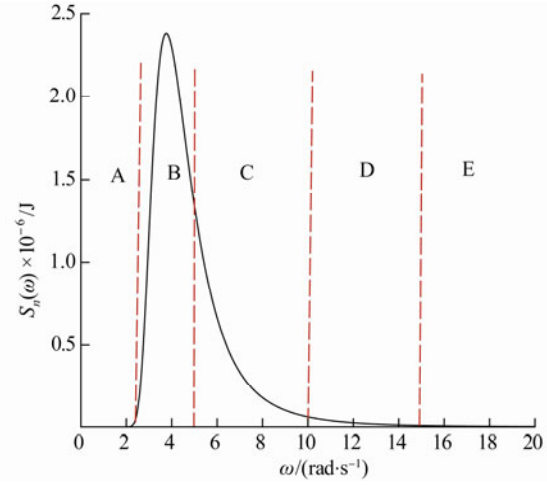


Fig. 22 Bretschneider excitation spectrum with $H_s = 0.01h_s$ and $\omega_p = \omega_1$

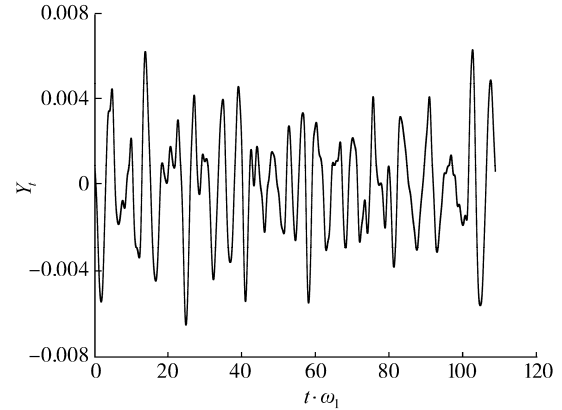


Fig. 23 Displacement generated from the spectrum

5.5.1 Selection of the linear angular frequencies (ω_i)

N_w denotes the number of linear waves superposed to create the random wave. In the present case, N_w is chosen to be 512 since such a high number ensures that a lot of frequencies within a given range contribute towards the generation of the random wave. The range of the angular frequencies is set as $[0, 5\omega_p]$ as the frequencies above $5\omega_p$ do not have a significant contribution towards the generation of the random wave. In the present case, ω_p is taken equal to the first natural frequency of the system ω which is 3.759 371 rad/s.

From Fig. 22, it is evident that in the energy spectrum, the wave energy (S_{ζ}) has the highest values around the modal or peak frequency (ω_p), hence a large number of angular frequencies were chosen in the narrow band around the value ω_p . Around 150 values of angular frequencies were

selected randomly in the range of [2.5, 5.0] which was a very narrow band around the peak frequency marked as A in Fig. 22 and B represents the range [0.0, 2.5] and 62 values of angular frequencies are selected randomly in this range. As can be seen from Fig. 22, the energies in this range were near to zero and hence have negligible contribution in the energy of the final generated random wave. Band C, D and E represent the ranges [5.0, 10.0], [10.0, 15.0] and [15.0, $5\omega_p$] and 100 values of angular frequencies were selected randomly in each of these ranges. The selection of linear angular frequencies within a range was done by using a floating random number generating algorithm that makes use of a fixed seed number and a custom built function $\text{rand}()$ (that gives the same set of random numbers every time for a fixed seed number). It is to be noted that the energy spectrum for angular frequencies above 10.0 rad/s falls well below 0.01×10^{-6} J, hence less number of angular frequencies were selected in this range. After the selection of angular frequencies, the amplitudes of the linear waves can be calculated by the following equation

$$A_i = \sqrt{2S_\zeta(\omega)\Delta\omega} \quad (81)$$

where $\Delta\omega$ is nothing but, the difference between adjacent angular frequencies ($\Delta\omega = \omega_{i+1} - \omega_i$).

5.5.2 Selection of the phase angle (ψ_i)

Using the same algorithm as used for selecting linear angular frequencies, N_w random values of phase angles were selected within the range $[0, 2\pi]$. By substitution of the selected random values of angular frequencies (ω_i), amplitudes (A_i) and phase angles (ψ_i) in Eq. (80), we can get the resultant random input wave. From Eq. (80), the vertically excited container displacements were obtained from this spectrum. The time history of surface elevation at LF_{3D} and RB_{3D} of the container due to random vertical excitation is shown in Fig. 24. Spectra of free surface sloshing waves at LF_{3D} of the wall due to vertical random excitation for an initial steepness of 0.288 and $\omega_p = \omega_1$. In the case of random excitation in vertical direction, the dominating peak appears only at the first mode (Fig. 25). The magnitude of the peak was almost the same irrespective of the excitation peak frequency and initial perturbation, contrary to the regular excitation. Sriram *et al.* (2006) found the magnitude was large only if the excitation frequency was

equal to twice the first mode (parametric resonance) irrespective of initial perturbation. Fig. 26 shows the surface plots for three conditions, say case C at $n=1$, $n=3$ and case D at $n=3$ from 32 to 35 non-dimensional time units with non-dimensional time step $\Delta t = 0.6$ units. The surface plots show a half cycle of wave's movement. The frames were shown for a wave steepness $K_x = 0.040$ 16.

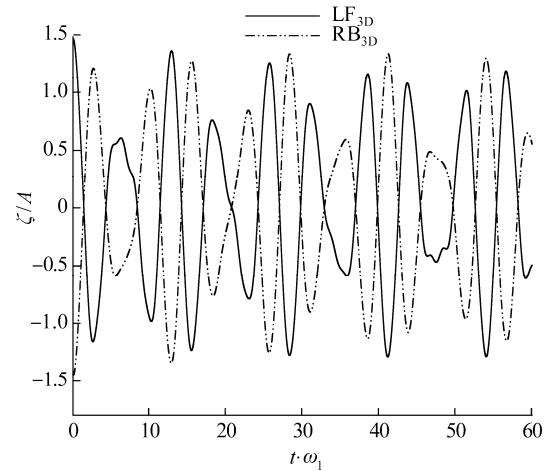


Fig. 24 Random vertically excited container free surface oscillation at LF_{3D} and RB_{3D} , for an initial steepness of 0.288; $\omega_p = \omega_1$

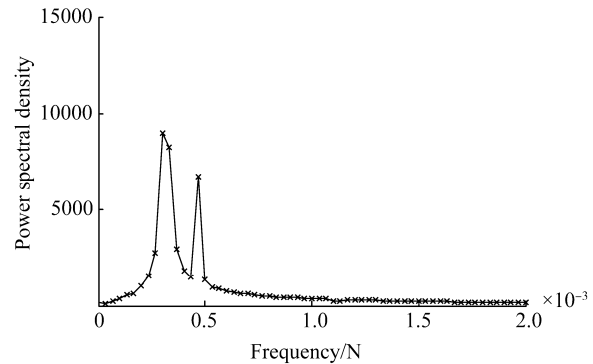
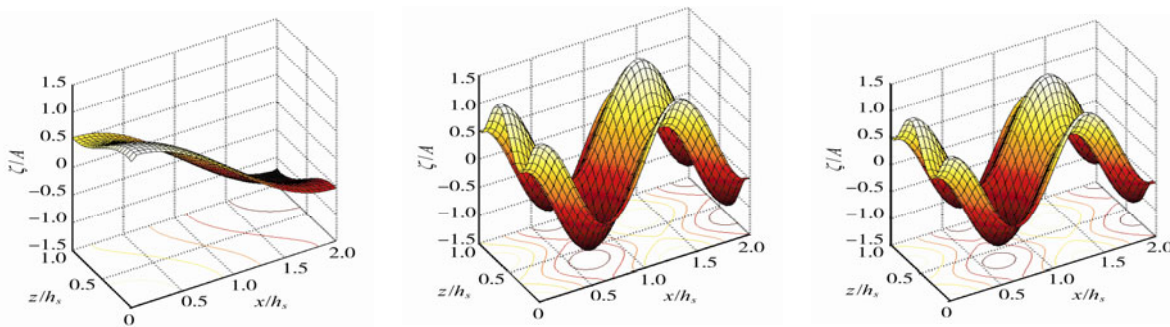


Fig. 25 Spectra of free surface sloshing waves at LF_{3D} of the wall due to vertical random excitation for an initial steepness of 0.288 and $\omega_p = \omega_1$



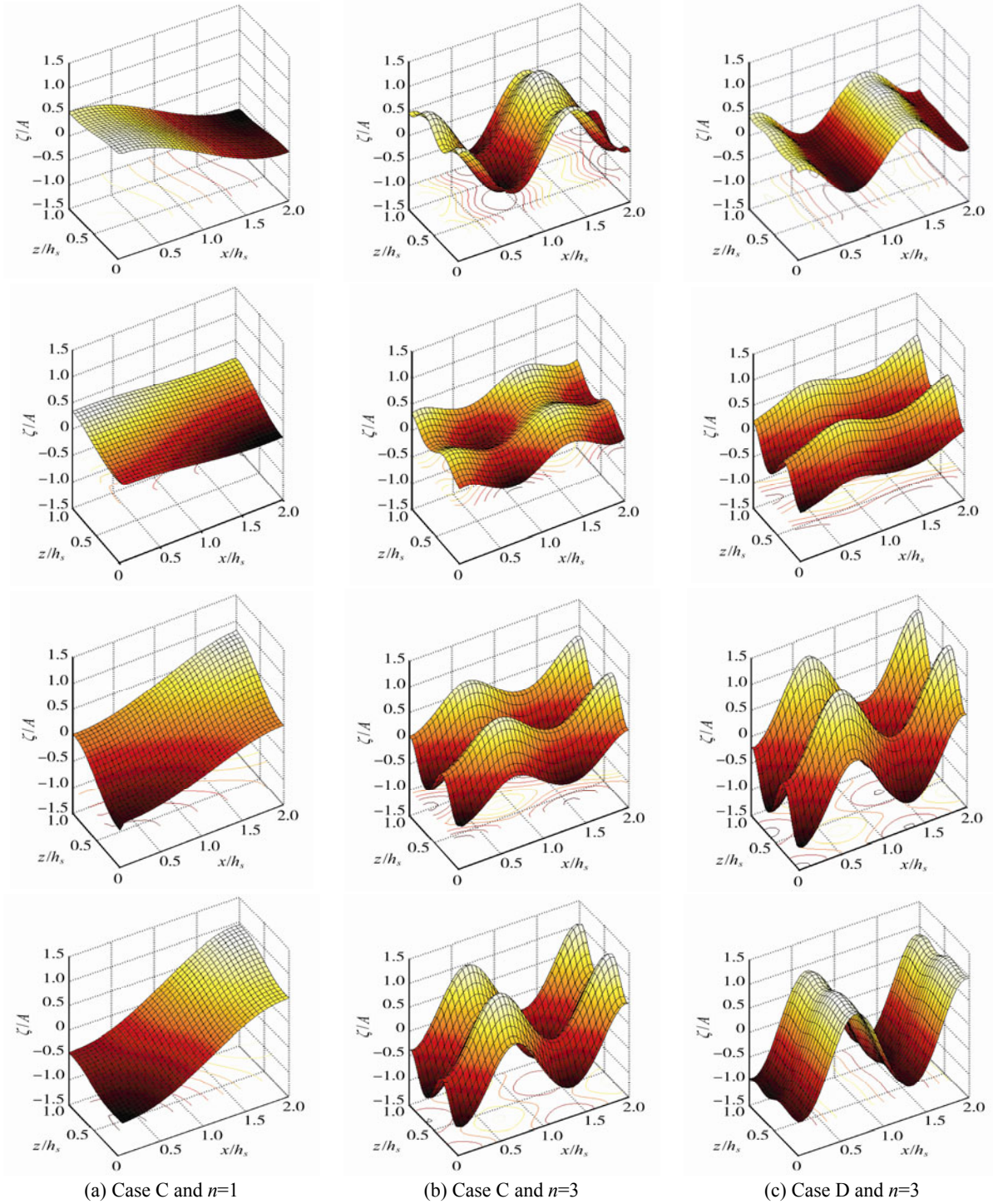


Fig. 26 Surface plot for different cases from the 32 to 35 non-dimensional time units with $\Delta t = 0.6$ time step

6 Conclusions

The proposed numerical model was found to be easy to implement, computationally accurate and efficient. In the cases presented herein, it eliminated the need for free surface smoothing and remeshing. The model provides a simple way of simulating steep non-breaking waves. The σ -transformation technique can be applied to

non-overturning and non-breaking waves. Present results were compared with the benchmark solutions of Faltinsen *et al.* (2000) (third order analytical solutions by multi modal technique). Non-linear effects of standing wave motion of liquid in 2D and 3D fixed and forced vertically regularly and randomly excited containers were studied numerically. The present study was carried out for regularly and randomly excited rectangular container in vertical direction for four different cases: 2D container with regular

excitations, the regularly excited 3D container with two different initial conditions for liquid free surface and finally, 3D container with random excitation in the vertical direction. A fully non-linear inviscid numerical model was developed based on potential flow theory with the mapped governing equations and corresponding boundary conditions solved using finite difference method. Results of liquid sloshing induced by harmonic base excitations were presented for small to steep non-breaking waves. The present numerical model was validated for use of any water depth, with the exception of shallow and deep water sloshing. An error estimation method was used to estimate the error for all iterations to serve as a basis for stopping the iterative solver when the steady state results are reached. The model was validated for different wave length and steepness. Good agreement was found between present and previously published theoretical solutions for the same type of test cases. The grid independence test showed that the grid size $41 \times 61 \times 41$ was efficient to solve the 3D sloshing problem in the given liquid container. Sloshing motion in vertically excited containers were carried out for the stable region conditions. Sloshing effects in a vertically excited container in stable regions display similar characteristics as free sloshing motions in a fixed container when the forcing parameter (K_v) is low. The phase plane diagrams showed the nonlinearity of the free surface waves with respect to time.

Initially, the wave elevation time history were observed for first few modes of sloshing on the free surface at the left wall for 2D regular (case A) and 3D regularly excited container with two initial profiles (case B and C) in vertical direction. The wave elevation time histories were plotted at different locations of the free surface. The wave elevation time history at a particular point on the free surface in the domain was then compared for cases A, B and C. Near the container wall the wave elevations were more due to the wall effect while the center of the container had low wave elevation profiles. The 2D and 3D container with initial profile 1 had similar wave elevation time history. If nonlinearity in the axial direction is increased by using profile 1 and 2 i.e. a linear superposition of two sinusoidal wave profiles, the 3D container will show a different wave elevation time history. The free surface elevation got the intricate shapes for the case C. Sloshing in randomly excited container in vertical direction was also studied. Bretschneider spectrum is selected to serve as the input excitation spectrum to generate the random input wave. The ratio of the excitation frequency and the natural frequency of the system (Ω_v) was kept as 1.253 in the study. Hence, the results reported were from the stable regions only.

Nomenclature

A	Wave amplitude
A_i	Wave amplitude of i th linear wave
A_x	Transverse excitation amplitude
b	Length of the container
DT''	Transverse acceleration of the container

E_b	Amplitude-length ratio ($=A/b$)
E_V	Volume error
g	Acceleration due to gravity
h	Instant water height from container bottom
h_s	Still water depth
H_s	Significant wave height
K_n, K_z	Wave numbers along the X and Z directions
K_v	Forcing parameter for vertical acceleration
K_x	Wave steepness
n	Mode number of oscillation
N_w	Number of linear monochromatic waves
t	Time
w	Axial width of the container

Greek symbols

ω_n, ω	Natural angular frequency of sloshing
ω_v	Angular frequency of vertical excitations
\ddot{Y}_t	Acceleration of the container in vertical direction
ψ_i	Phase angle of i th linear wave
ω_i	Frequency of i th linear wave
ω_p	Modal or peak frequency of the wave spectrum
S_ζ	Wave energy due to Bretschneider spectrum
δ^n	Iteration error at n^{th} iteration
ζ	Free-surface elevation
σ	Grid Stretching Factor
$\phi(x, y, t)$	Velocity potential function in physical domain (x, y, t)
$\Phi(X, \sigma, T)$	Velocity potential function in computational domain (X, σ, T)
δ, δ^2	First and second order central difference operators
λ_1	Spectral radius or the largest eigen value of the iteration matrix
Y_t	Container displacement
$\delta_\xi \delta_\eta$	Mixed second order central difference operator
Ω_v	Frequency ratio $= \omega_v / \omega$; ω is the natural sloshing frequency and ω_v is the angular frequency of vertical excitations.

References

- Akyildiz H, Unal N (2006). Sloshing in a three-dimensional rectangular container: numerical simulation and experimental validation. *Ocean Engineering*, **33**(16), 2135-2149.
- Arafa M (2007). Finite element analysis of sloshing in rectangular liquid-filled containers. *Journal of Vibration Control*, **13**(7), 883-903.
- Blumberg AF, Mellor GL (1980). A coastal ocean numerical model. *Mathematical Modeling of Estuarine Physics, Proceedings of an International Symposium*, Berlin, 203-219.
- Chen BF, Nokes R (2005). Time-independent finite difference analysis of fully non-linear and viscous fluid sloshing in a rectangular

- container. *Journal of Computational Physics*, **209**(1), 47-81.
- Chern MJ, Borthwick AGL, Taylor RE (1999). A pseudospectral σ -transformation model of 2-D nonlinear waves. *Journal of Fluids and Structures*, **13**(5), 607-630.
- Cho JR, Lee HW, Ha SY (2005). Finite element analysis of resonant sloshing response in 2D baffled container. *Journal of Sound Vibration*, **288**(4/5), 829-845.
- Dai L, Xu L (2006). A numerical scheme for dynamic liquid sloshing in horizontal cylindrical containers. Proceedings of the institution of mechanical engineers, Part-D. *Journal of Automobile Engineering*, **20**(7), 901-918.
- Eswaran M, Saha UK (2009a). Low steeping waves simulation in a vertical excited container using σ -transformation. *28th International Conference on Ocean, Offshore and Arctic Engineering*, Honolulu, USA, OMAE 2009-80248.
- Eswaran M, Saha UK (2009b). Numerical simulation of low steeping waves in a horizontally excited container using sigma transformation. *Proceedings of the 3th International Congress on Computational Mechanics and Simulation (ICCMS-09)*, Bombay, India, M27.
- Eswaran M, Saha UK (2010). Waves simulation in an excited horizontal cylindrical container using σ -transformation. *ASME International Mechanical Engineering Congress & Exposition*, Vancouver, Canada, IMECE 2010-39752.
- Eswaran M, Saha UK, Maity D (2009). Effect of baffles on a partially filled cubic container: Numerical simulation and experimental validation. *Computers and Structures*, **87**(3/4), 198-205.
- Eswaran M, Singh A, Saha UK (2011). Experimental measurement of the surface velocity field in an externally induced sloshing tank. *Proceedings of the Institution of Mechanical Engineers, Part M: Journal of Engineering for the Maritime Environment*, **225**(3), 133-148.
- Faltinsen OM (1974). A nonlinear theory of sloshing in rectangular containers. *Journal of Ship Research*, **18**(4), 224-241.
- Faltinsen OM, Rognabakke OF, Lukovsky IA, Timokha AN (2000). Multidimensional modal analysis of nonlinear sloshing in a rectangular container with finite water depth. *Journal of Fluid Mechanics*, **407**, 201-234.
- Faltinsen OM, Timokha AM (2002). Asymptotic modal approximation of nonlinear resonant sloshing in a rectangular container with small fluid depth. *Journal of Fluid Mechanics*, **470**, 319-357.
- Faraday M (1831). On a peculiar class of acoustical figures, and on certain forms assumed by groups of particles upon vibrating elastic surfaces. *Phil Trans R Soc Lond.*, **121**, 299-340.
- Ferziger JH, Peric M (2002). *Computational methods for fluid dynamics*. 3rd rev. edition, Springer-Verlag, Berlin, Heidelberg, New York.
- Frandsen JB (2004). Sloshing in excited containers. *Journal of Computational Physics*, **196**, 53-87.
- Frandsen JB, Borthwick AGL (2003). Simulation of sloshing motions in fixed and vertically excited containers using a 2-D inviscid σ -transformed finite difference solver. *Journal of Fluids and Structures*, **18**, 197-214.
- Graham EW, Rodriquez AM (1952). Characteristics of fuel motion which affect airplane dynamics. *Journal of Applied Mechanics*, **19**(3), 381-388.
- Hill DF (2003). Transient and steady-state amplitudes of forced waves in rectangular basins. *Physics of Fluids*, **15**(6), 1576-1587.
- Hirt CW, Nichols BD (1981). Volume of fluid (VOF) method for the dynamics of free boundaries. *Journal Computational Physics*, **39**(1), 201-205.
- Housner GW (1957). Dynamic pressures on accelerated fluid containers. *Bulletin of the Seismological Society of America*, **47**(1), 15-35.
- Housner GW (1963). The dynamic behavior of water containers. *Bulletin of the Seismological Society of America*, **53**(2), 381-387.
- Ibrahim RA (2005). *Liquid sloshing dynamics: Theory and applications*. 1st ed. Cambridge University Press, New York.
- Jacobsen LS, Ayre RS (1951). Hydrodynamic experiments with rigid cylindrical containers subjected to transient motions. *Bulletin of the Seismological Society of America*, **41**(4), 313-346.
- Maleki A, Ziyaeifar M (2008). Sloshing damping in cylindrical liquid storage containers with baffles. *Journal of Sound and Vibration*, **311**, 372-385.
- Mellor GL, Blumberg AF (1985). Modeling vertical and horizontal diffusivities with the sigma coordinate system. *Monthly Weather Review*, **113**, 1379-1383.
- Phillips NA (1957). A coordinate system having some special advantages for numerical forecasting. *Journal of Atmospheric Sciences*, **14**, 184-185.
- Popov G, Sankar S, Sankar TS, Vattistas GH (1993). Dynamics of liquid sloshing in horizontal cylindrical road containers. *Proceedings of the Institution of Mechanical Engineers, Part C: Journal of Mechanical Engineering Science*, 207-C6, 399-406.
- Sriram V, Sannasiraj SA, Sundar S (2006). Numerical simulation of 2D sloshing waves due to horizontal and vertical random excitation. *Applied Ocean Research*, **28**, 19-32.
- Turnbull MS, Borthwick AGL, Taylor RE (2003). Numerical wave container based on a σ -transformed finite element inviscid flow solver. *International Journal for Numerical Methods in Fluids*, **42**, 641-663.
- Wang CZ, Khoo BC (2005). Finite element analysis of two-dimensional nonlinear sloshing problems in random excitations. *Ocean Engineering*, **32**, 107-133.

Author biographies



Eswaran M received his PhD in Mechanical Engineering from Indian Institute of Technology Guwahati, India in 2011. Currently, he is working as a Research Associate in Bhaba Atomic Research Centre, Trombay, Mumbai, India under KSKRA Fellowship Scheme. His areas of research interest include slosh dynamics, fluid-structure interactions, computational and experimental fluid dynamics.



Akashdeep S. Virk received his Bachelor of Technology in Mechanical Engineering from Indian Institute of Technology Guwahati, India in 2010. Currently, he is a research intern in the Department of Mechanical Engineering, National University of Singapore, Singapore. His areas of research interest include slosh dynamics, computational and experimental fluid dynamics.



U. K. Saha received his PhD in Aerospace Engineering from Indian Institute of Technology Bombay, India in 1996. Currently, he is a professor in the Department of Mechanical Engineering, Indian Institute of Technology Guwahati. His broad areas of research include internal combustion engines, wind energy, compressor aerodynamics, propulsion and slosh dynamics. He is currently often invited as a reviewer of many international journals and conferences. He has supervised several R&D and consultancy projects. He is an ASME member.